DESIGN AND TESTING OF KINETIC ENERGY PENETRATORS

S. Burnage *

Abstract

This paper reports on the design and testing of instrumented *Kinetic Energy Penetrators* (KEPs). The behaviour of such devices in response to penetration into various targets is analysed. Prototypes have been developed at INSYS for application on Mercury and Mars Lander missions plkanned by the European Space Agency ESA. The test results show that kinetic energy penetration devices may be a suitable way to explore the uppermost metres of planetary surfaces.

1 Introduction

The work presented in this paper has centred on extensive studies into the use of *Kinetic Energy Penetrators* (KEPs) for use in both military and civil space applications. Both use instrumented KEPs to monitor the response characteristics during penetration of different target types, over a range of velocities and orientations. The KEPs must be capable of containing, protecting, initiating and transferring data collected from on–board instrumentation.

Over the last decade, INSYS have been involved in the design, development, testing and analysis of a range of instrumented KEPs for military applications with the objective of defeating heavily protected static targets. In addition, extensive studies have been performed on the use of KEPs in civil space applications for the European Space Agency to deploy sub–surface experiments on Mars (*MarsNet*) and Mercury (*BepiColombo*).

In all studies, the work initially concentrated upon the design and structural analysis of the KEPs in terms of their ability to penetrate targets and offer protection to the on–board instrumentation. Extensive shock testing and attenuation studies were performed. Prototypes were then manufactured and tested within the high–energy gas gun facility at INSYS to investigate penetration and impact resilience performance.

* *Technologies–Future Concepts, Lockheed Martin UK Insys Ltd., Ampthill, UK, Email: steve.burnage@insys-ltd.co.uk*

2 KEP study

INSYS has undertaken a series of inter–related work programmes aimed at developing compact instrumented penetrators, which can defeat heavily protected static targets. The data acquired from the trials programme were used for the development of fuzing systems capable of identifying the onset of target perforation. Within this study a general–purpose projectile that was capable of penetrating a range of target types — including single and multiple layers — was designed and developed. The penetrator also protected an on–board solid–state data recorder, battery and sensor. In the development of the penetrator, parametric models were used to investigate the interaction of different designs with a range of target configurations. The penetrator selected for the trials programme was based upon this interactive modelling study.

A series of penetration trials were performed using instrumented penetrators to obtain acceleration signatures against a range of single and multiple targets. An important feature of this study was the examination of the effects on the captured penetration/perforation signal to variations in sensor location within the projectile. Combining this data with the results from modal testing and Finite Element (FE) models, enabled the affects of data transportation to be addressed i.e. fidelity of measured results against sensor location within the penetrator.

The analysis of the recorded acceleration data, both in the time and in the frequency domain, identified signature components that were dominated by the effects of impact excitation and penetrator structural response. Quantifiable trends due to variations in target types and penetrator impact speeds were also observed for possible use in fuzing algorithms.

2.1 Penetrator analysis

The penetration analysis employed for this investigation was based upon parametric models of the target/penetrator interaction. The requirement to investigate a large number of conditions, representing different target characteristics and optimisation of penetrator design precluded the use of high order modelling methods — such as hydrocodes. The selected techniques provided an efficient and cost-effective approach, which matched the remit of the study to develop a simple and compact penetrator.

Initial studies considered the use of semi-empirical codes based upon the SANDIA–equations derived by Young (1982). These equations are based upon data obtained from over 500 full–scale penetration tests into a variety of targets, including rock, ice, sand and saturated clay. The penetration equations were derived for two different velocity regimes:

$$P = 6.080 \times K \times S \times N\sqrt{(M/A)} \times \ln(1 + 2.15 \times 10^{-4}\, V^2) \qquad V < 61\text{m/s}$$

$$P = 0.117 \times K \times S \times N\sqrt{(M/A)} \times (V - 30.5) \qquad V > 61\text{m/s}$$

where the variables have the variables have the following meaning:

P – penetration depth in [m]
V – impact velocity in [m/s]
M – mass in [kg]
A – cross sectional area in [m^2]
S – 'soil constant' (dimensionless)
K – weight scaling (dimensionless)
N – nose shape coefficient (dimensionless)

The accuracy of these equations is strongly dependent upon the accuracy with which the soil constant S can be determined. Within a restricted range, and with appropriate choice of parameters, the equations are capable of giving reasonably accurate estimates of penetration depth. Moreover, by differential analysis, insight into rigid body deceleration profiles can be gained. A fit matching the experimental data within ±20% is generally considered to be a good result.

Another method to describe the penetration event is to use an analytical method where the equation of motion for the penetrator is expressed in terms of target resistive forces and solved by direct integration for successive time steps, using numerical techniques. The target penetration algorithm was based upon soil mechanics equations for end bearing resistance, dynamic shaft adhesion and confining pressure. The target resisting force is given by:

$$F = W - q_b \times A_x - q_s \times A_s - q_c \times A_x$$

with

W – weight of penetrator in [N]
q_b – end bearing stress in [N/m^2]
q_s – shaft adhesion in [N/m^2]
q_c – confining pressure in [N/m^2]
A_x – cross sectional area of penetrator in [m^2]
A_s – contact surface area of penetrator in [m^2]

The prediction of target penetration using this method was validated against SANDIA results. Some eighty tests were used to validate the model, covering a wide range of impact velocities, penetrator masses and diameters for differing target types.

Both of the analytical methods were combined with a lumped mass model of the penetrator (Figure 1), which had the appropriate mass, centre of gravity and moment of inertia. The model represents the rigid body behaviour of the penetrator during impact and penetration. Angled impacts were modelled by specifying initial impact orientation and velocity vectors, with the penetrator being reacted against the target resistive forces given by the penetration equations. Since for angled impacts, the axial penetration, lateral translation and pitch angle rotation of the penetrator can be large (particularly for impacts into sand/soil overburdens), then a large displacement method is used for

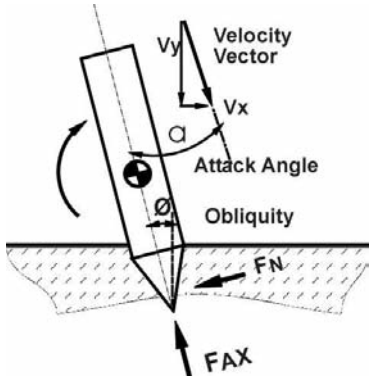

Figure 1: Target penetration model.

the transient dynamic analyses, in which the equations of motion are solved by direct integration.

The analysis was used to examine the influence of various parameters on the penetration process, including changes to nose shape, diameters and stepped profiles (Burnage and Waine, 1993). The temporally distributed forces acting along the penetrator body length was applied to a more refined FE model of the penetrator to assist in its structural characterisation.

2.2 Penetrator design

The penetrator was of conventional design (Figure 2) and was essentially a hollowed 60 mm diameter steel rod with a solid forebody and a conical nose. The total mass of the penetrator, as fired, was approximately 5 kg. The hollow main section housed the instrumentation, with a single accelerometer mounted either at the rear of the solid section or in the rear end cap. The forward mount location offered the potential to monitor the effects of the penetration process clearly, with relatively little contamination from the response characteristics of the penetrator. The aft mounted transducer (practicable for fuzing applications) as expected, was greatly influenced by the dynamic response of the penetrator.

The instrumentation package contained an accelerometer, an interface to the solid–state recorder (User Manual, 2002) and a potted 12 V battery assembly and interface circuitry. In addition, the instrumentation cavity was pressurised with a glass bead compound to act as a support and to mitigate shock effects on the instrumentation.

2.3 Trials configuration

A high energy airgun (Figure 3) was used to accelerate the penetrators up to velocities between 200 m/s and 270 m/s. The airgun comprised of a 31 bar air reservoir and a Ø165 mm

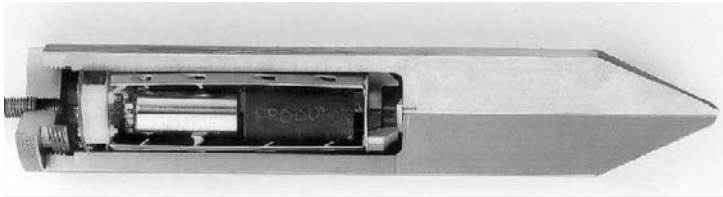

Figure 2: Penetrator and instrumentation package.

aluminium barrel. A nylon sabot was used to support the penetrator in the barrel and this was separated from the penetrator prior to target impacting a sabot–stripping plate. The targets were 750mm×750mm reinforced concrete slabs with a thickness of 200 mm for the single targets and 100 – 150 mm for the multiple targets. After target perforation, the penetrators were retrieved from a sand butt and disassembled; the data recovered from the recorders via a laptop and interface box.

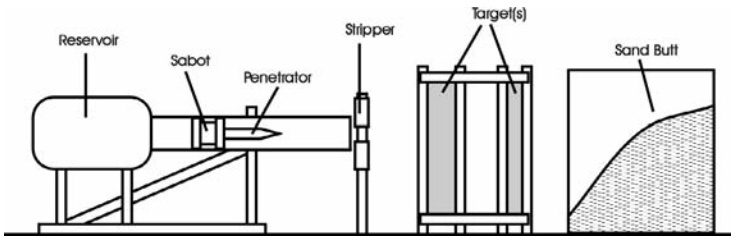

Figure 3: Airgun test configuration.

2.4 Data analyses

Analysis was performed on the measured data in both time and frequency domains. The identification and quantification of characteristics within the data that may 'flag' the onset of perforation, was a primary objective. The identification of any 'unique' characteristic that may originate from either a failure mechanism of the target and/or the dynamic response of the penetrator were of particular interest.

2.5 Time domain

Data analyses within the time domain yielded information related to the loading history applied to each target configuration and its associated penetrator. Typical traces from the forward mounted location (Figure 4) show a clearly distinguishable high frequency response superimposed upon a much lower 'rigid–body' deceleration profile. The peak amplitude of the rigid body response for this particular range of target configurations was approximately 16000 g. The high frequency, high amplitude responses (35000 g) are

produced by a combination of penetrator flexible body modes, penetrator stress wave propagation and external excitations produced by target failure responses.

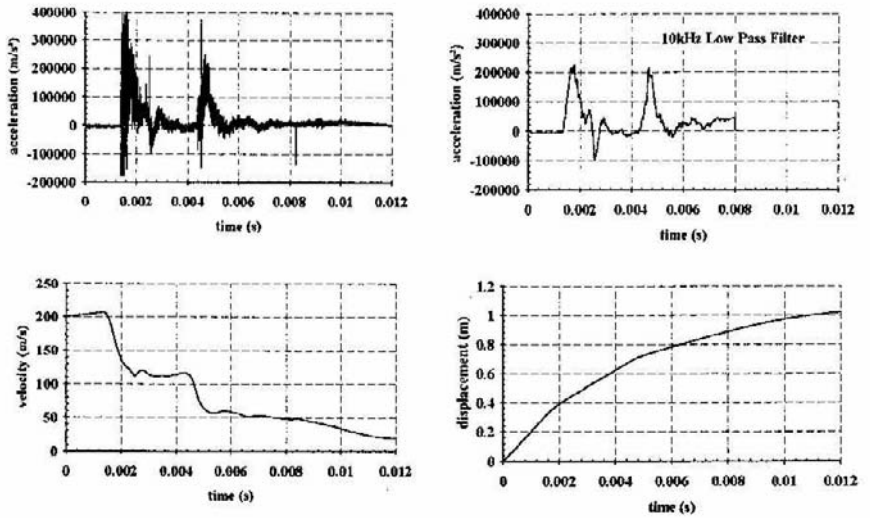

Figure 4: Acceleration/velocity/displacement time history.

The high frequency component of the data was removed using a 10 kHz low pass filter to investigate the 'rigid–body' response of the penetrator. The results show a combination of target failure (front face scabbing and rear face spalling), coupled with at least one flexible body penetrator mode. To assess data fidelity, unfiltered acceleration time histories were numerically integrated to give both penetrator velocity and displacement time histories. The results compared favourably with predicted target perforation times and independently measured exit velocities.

2.6 Frequency domain

To identify and track selected modes during the penetration and post perforation period, a frequency domain analysis was performed on the data. As the projectile impacts the target and commences penetration, its boundary conditions change from free flight to essentially those of a constrained 'cantilever' beam. Conversely, as the projectile perforates, its boundary conditions revert to free flight conditions. It is the potential to identify the effects on penetration of these variations in constraint conditions that justified undertaking analyses in the frequency domain.

A pair of frequency spectra representing the penetration and post perforation phases of a typical event is presented in Figure 5. Unfortunately the resolution is poor (0.5 kHz) and consequently, the values highlighted should be used with caution. However, a general

change in frequency distribution between the penetration and post perforation can be identified. During penetration, there is a trend to excite even numbered modes (second bending), whilst post perforation responses show a migration to odd numbered modes (first bending & first axial).

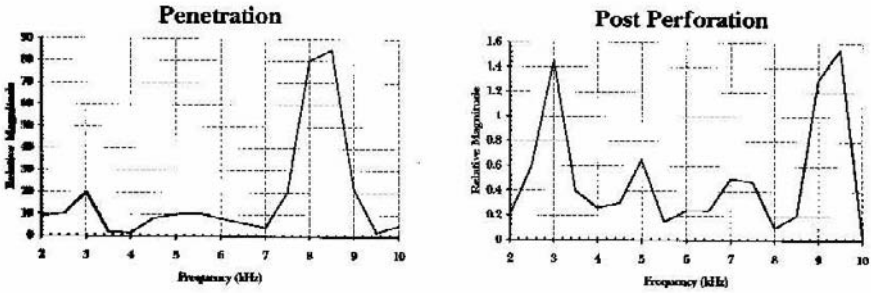

Figure 5: Frequency domain.

2.7 Data transportability

The effects of variations in sensor location within a penetrator on measured and/or predicted acceleration responses are of prime interest within this phase of the study. The objective was to assist fuze designers in the prediction of acceleration environments at any practicable sensor location based upon measurements derived at some other position on a penetrator. In undertaking such data 'transportation', due account must be taken of any future penetrator body design and sensor mounting configuration as determined by its modes of excitation.

The accelerometers attached directly to the fore–section of the penetrator produced acceleration responses that were (as expected) only minimally affected by penetrator characteristics. Consequently, it is likely that small changes in transducer location would have little effect on measured response. Practical operational fuzing requirements will almost certainly call for sensors to be located at the rear of a penetrator. However, accelerometers mounted at the rear of a penetrator are significantly affected by penetrator dynamics response characteristics. This will imply that measured responses will be greatly affected by small changes in sensor location. The measured axial response of a front and rear mounted accelerometer impacting and perforating identical multiple targets is shown in Figure 6.

A significant increase in magnitude and duration of vibratory response following initial impact can be seen for the accelerometer located in the rear endcap. This was particularly prevalent during second target penetration in which an increase in impact angle of obliquity, following first target perforation, exacerbates the rear sensor response.

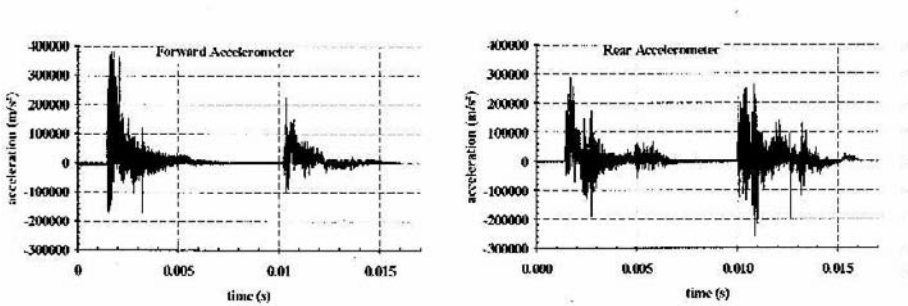

Figure 6: Front & rear responses.

To investigate the relative distribution in dynamic response of the projectile along its length, a pendulum impact test was performed on a penetrator that contained four accelerometers. Pairs were orientated longitudinally and laterally in the front and rear penetrator. An FE model replicating the modal characteristics of the penetrator was subjected to an identical transient excitation and the predicted responses at corresponding front and rear sensor locations computed. Results from the modal test and model correlated in terms of amplitude — although modal model decay rates were rather poor, indicating that the model damping characteristics required further refinement. The peak axial and lateral accelerations, as predicted by the model, were extracted at various stations along the length of the penetrator body and then normalised with respect to the forward accelerometer response. The plots of the distributions (Figure 7) show a good indication of 'transportation'.

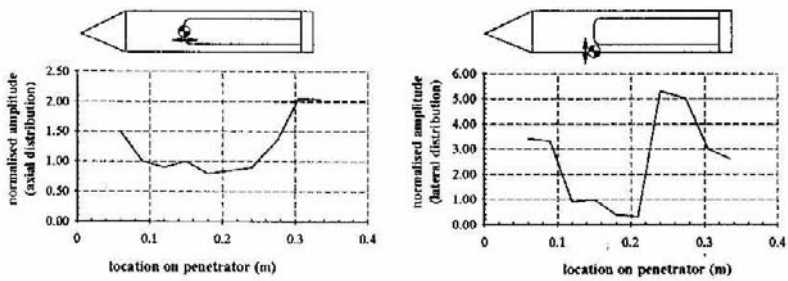

Figure 7: Acceleration amplification distribution.

Axial distributions show that the peak responses at the rear of the penetrator are double those experienced at the forward location. A similar magnification is also seen in the lateral direction. However, the later response of the hollow section has increased by up to five fold – this is attributed to the localised 'ringing' modes of the penetrator. Thus, by applying either measured or theoretical transient loading conditions to a validated penetrator modal model, a fuze designer can select potential sensor sites from the responses

predicted by the model. The influence of mounting the fuzing device at the preferred location on the penetrator could be assessed by refining the modal model to include the detail design of the fuze assembly.

3 Planetary probes

INSYS has been involved with the European Space Agency in the design and development of two probe concepts, namely a hard lander probe for Mars and a surface element for Mercury. Both probes rely upon dissipating kinetic energy upon impact by a combination of surface penetration and controlled structural deformation.

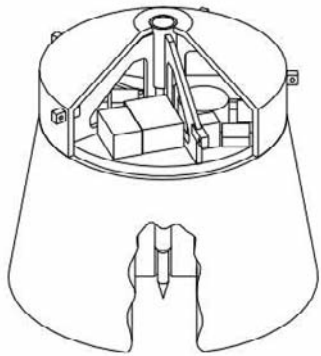

Figure 8: ESA MARSNET hard lander.

3.1 Mars probe

The Mars hard lander concept upon impact, allows the forebody (penetrator) to perforate the surface, whilst the aftbody remains on the surface, as it contains the communications, optical and meteorological instrumentation (Figures 8 and 9).

The forebody contains solid–state instrumentation, which is connected to the aftbody via an armoured umbilical chord. The solid–state devices have the ability to withstand very high shock–loading environments (over 200000 g) as demonstrated in the military KEP studies. The aftbody attenuates the impact loading to protect the more sensitive scientific equipment. This is achieved by the use of an aluminium honeycomb skirt, which is able to progressively crush, and by doing so, control the resultant payload deceleration levels. Typical crushing characteristics of honeycomb are shown in Figure 10. By using pre–crushed honeycomb, the initial high resistance force is eliminated, and a uniform crushing force can be maintained. Honeycomb typically 'blocks–out' at 75% of its original length.

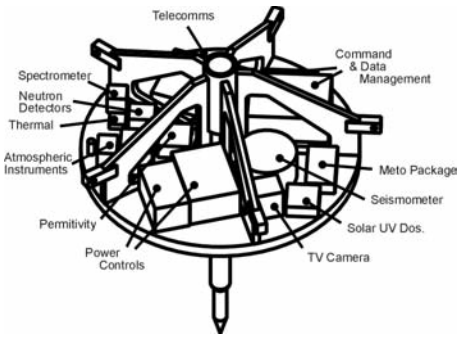

Figure 9: Aftbody payload section.

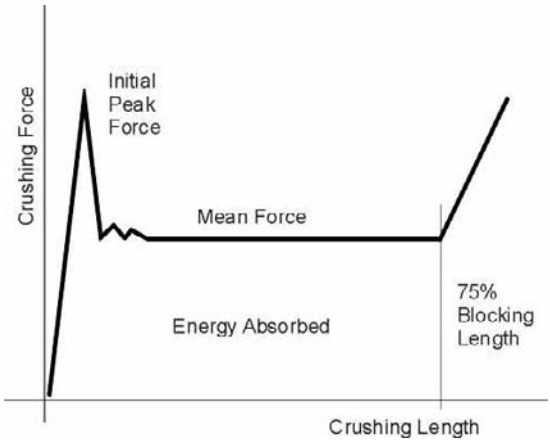

Figure 10: Honeycomb crush characteristics.

The resultant rigid body deceleration loads acting on the equipment section can be simply derived using:

$$Deceleration = Crush\ Force\ /\ Payload\ Mass$$

The amount of kinetic energy that can be absorbed by the honeycomb is a function of its mean crushing force and 'blocking distance', see Figure 10 (1 Nm = 1 Joule). Therefore, knowing the impact velocity and mass of the probe, it is possible to select the type of honeycomb and volume required to absorb the impact energy. The probe mass was 60 kg, and predicted to impact the surface of Mars at a velocity not exceeding 85 m/s. This equates to a kinetic energy of 216 kJ. Selecting a commercially available aluminium honeycomb with a mean crushing strength of 620 kN/m^2, and a contact area of 0.64 m^2, results in a crushing force of 396 kN. To completely absorb all of the available kinetic

energy, the required depth of honeycomb skirt is 0.73 m:

$$\textit{Skirt Depth} = \textit{K.E.} /(\textit{Crush Force x } 0.75)$$

With a probe mass of 60 kg, the predicted mean rigid body deceleration is therefore 660 g (Earth).

3.2 Impact studies

A lumped mass model was generated using the ISIM interactive simulation language code (International Simulation Limited, 1992) in which the payload platform, the forebody penetrator and their interaction with various grades of surface resistivity (drift, compacted sand and basalt) were represented. This model was used to define the impact performance envelope in terms of impact attitude, soil types and surface slopes (Figure 11).

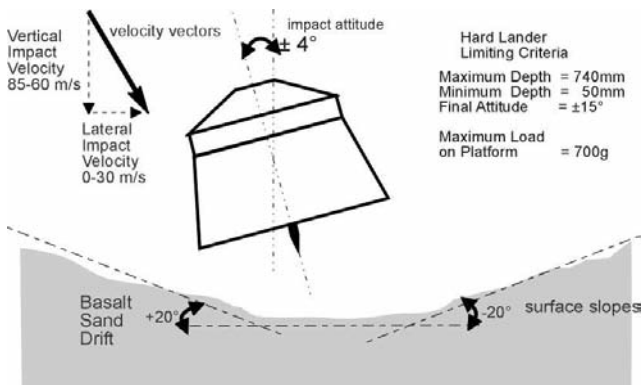

Figure 11: Impact parameters.

The baseline impact response for the platform was confirmed as being a vertical impact into basalt at a velocity of 80 m/s. The payload platform rigid body response is shown in Figure 12.

3.3 Mercury probe

The Mercury Surface Element has an aft– and a forebody as its central core (Figure 13). The aftbody contains all the geochemical experimentation, cameras, power supplies and communication. The forebody holds the geophysical experiments and is connected to the aftbody via an umbilical chord.

Two (split launch option) solid propellant motors are attached to the aftbody structure. The smaller is used to insert the MSE into a ballistic entry trajectory, the second controls the descent velocity of the MSE. At a given height, lateral thrust motors rotate the MSE

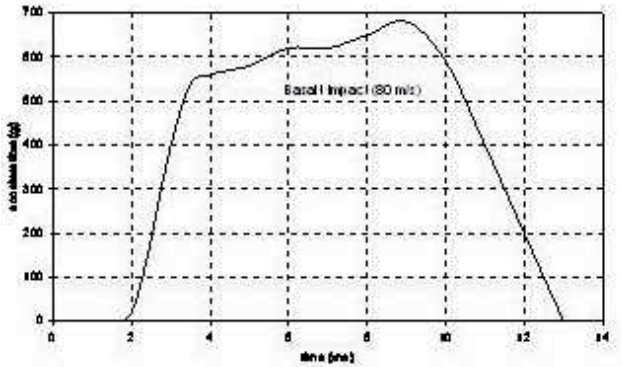

Figure 12: Payload platform impact loading.

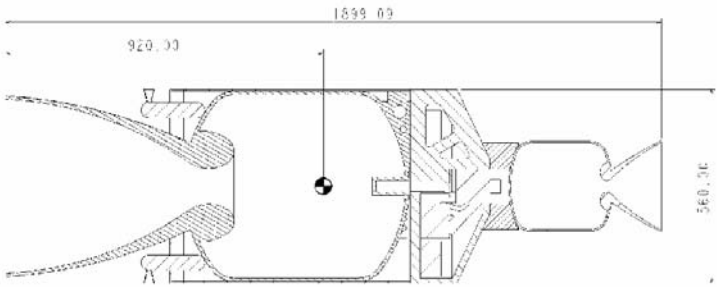

Figure 13: Mercury Surface Element assembly.

so that it is orientated vertically, and then the MSE is allowed to free fall. The axial crushing of the main motor casing controls aftbody deceleration load, whilst the forebody is free to impact and penetrate the surface of Mercury under its own inertia (Figure 14).

The mass prior to impact is 63.8 kg, which from a free fall drop height of 1.5 km equales to an impact energy level of 351 kJ at an impact velocity of 105 m/s. Upon impact, the motor casing/nozzle is utilised as the main energy absorption device. It is constructed as a filament wound carbon composite, whose thickness (2 mm) and fibre orientation is optimised to withstand the internal pressurisation during motor burn and yet readily deform under the axial impact loading. The collapse force is governed by the 2500 m/s^2 deceleration loading imposed on the aftbody. Similar devices have already been constructed and tested at INSYS (Figure 15).

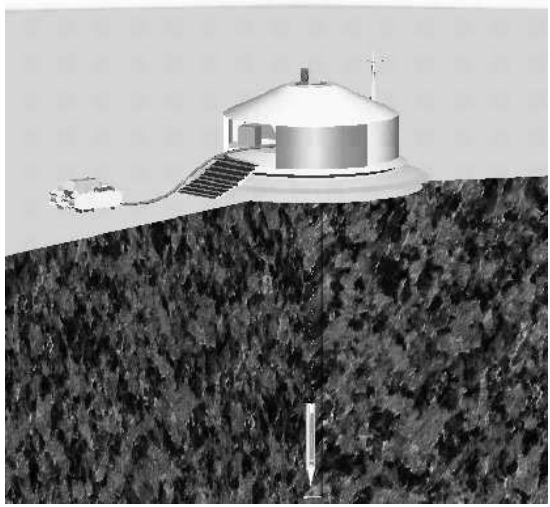

Figure 14: Aftbody on the surface with forebody buried in the ground.

Figure 15: Motor casing impact crush.

3.4 Aftbody

The aftbody is constructed from aluminium honeycomb, skinned with carbon fibre, making the structure light weight with high stiffness. All the scientific equipment, control and communication packages are attached to the main platform (Figure 16). The base of the equipment platform is connected to the descent motor casing. The main structural support is through three radial webs (carbon fibre skinned aluminium honeycomb core), which support the external skins and the internal core supporting the forebody penetrator.

The microrover restraints are incorporated into the aftbody, and their release simultaneously activated along with the opening of the access panel located in the sidewall and the

Figure 16: Equipment platform on aftbody.

deployment of the communications antennae. The designs of these devices were performed by students from two local schools under the INSYS sponsored Engineering Education Scheme (Deployment of Micro Rover Access Panel, 2000). The microrover is free to exit the aftbody, and must be capable of surviving a fall from a drop height of 0.2 m (Figure 17). The microrover is connected to the MSE via a spoolable umbilical cable. There is the potential to transport the magnetometer, using the microrover, to some 1.5 m distance from the aftbody. It will be connected by an umbilical cable and simply allowed to free fall from the Rover onto the surface. The rotating panoramic camera will be positioned on the top of the aftbody cone, inside the well of the forebody penetrator support structure.

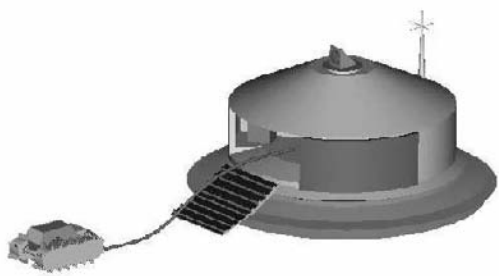

Figure 17: Deployed aftbody.

3.5 Forebody

The forebody shall be retained within the aftbody central support hub–enveloped by the main rocket initiator. Due to high thermal loads, the penetrator shall be protected by an additional layer of intumescent material that has the capacity of limiting the temperature of the penetrator to below 100°C. The penetrator is manufactured from a hollow titanium structure into which the geophysics packages are integrated (Figure 18). The forebody is

connected to the aftbody data handling and storage equipment by means of an armoured spoolable umbilical chord.

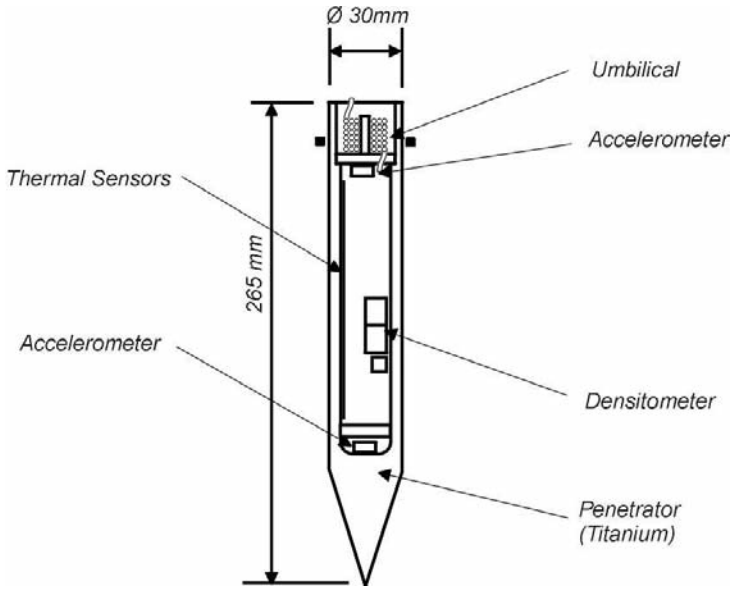

Figure 18: Forebody.

As the aftbody decelerates on impact, the inertia forces acting on the forebody are more than sufficient to fail the shear–limited restraints (nominally set at 500 m/s^2). Once separated, the forebody is free to pass through the deforming motor casing/nozzle, then impact and penetrate the surface of the planet. Its impact orientation being essentially governed by its original velocity vector and angle of incidence. The penetration performance of the forebody into regolith is presented in Figure 19. It shows that from an original free fall height of 1.5 km, the penetrator is capable of reaching a depth of about 7.3 m, with a mean rigid body deceleration loading of 2400 m/s^2.

4 Shock testing

In addition to studying the effects of high energy penetration, the equipment installed within the aft body had to be assessed and tested against transmitted shock loadings induced during the impact phase of the mission. The testing of items to withstand high amplitude shocks, such as those experienced by high velocity impacts (80 – 100 m/s) and surface penetration, requires the use of equipment that can impart considerably higher levels of energy into the component under test. The equipment must have the capability to control both amplitude and duration of the required loading transient, along with the ability to produce the desired shock profile.

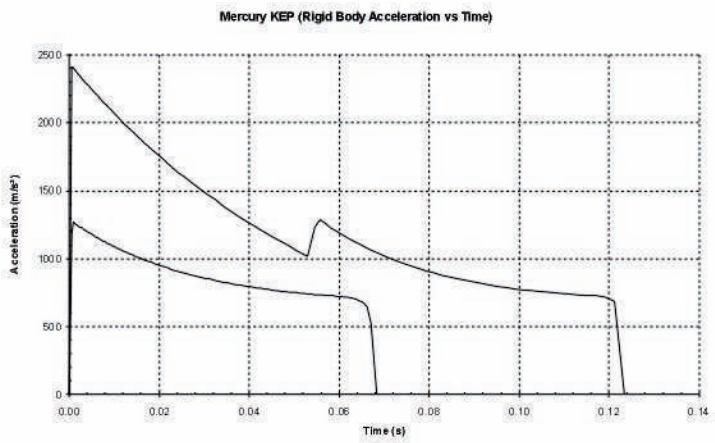

Figure 19: Penetrator performance curves.

Several methods exist, and they broadly fall into three categories, namely: electromagnetic accelerators, air/vacuum guns and controlled explosive devices. All rely upon accelerating a projectile, or payload, to a high velocity prior to imparting a controlled impact, which generates the large accelerations and durations required. Of these devices, the airgun is by far the simplest one to construct, operate and control.

4.1 Impact testing

The general configuration of the airgun was to propel an inert projectile by air pressure down a gun barrel to impact a test piece (anvil). After impact, the anvil is brought to rest relatively gently by use of a catcher system (rag box, sand butt or honeycomb arrestor). The impact of rigid bodies made from metal can result in very high peak accelerations that are generated for only very short durations (typically 100000 g for 30 μs). To extend the duration of the applied loading transient requires inserting a 'shock profiler' of lower stiffness and mass between the projectile and the anvil (Figure 20).

If the profiler is assumed to behave elastically, both the amplitude and duration of the applied pulse can be calculated for a specific set of impact conditions (Burnage and Waine, 1993)). Assuming that the acceleration/time history of the anvil is essentially a half–sine pulse, then the duration of this pulse (τ) is a function of the ratio of the two impacting masses (M_1 and M_2) and the profiler stiffness (K):

$$\tau = \pi \sqrt{\frac{M_1\ M_2}{K(M_1 + M_2)}}$$

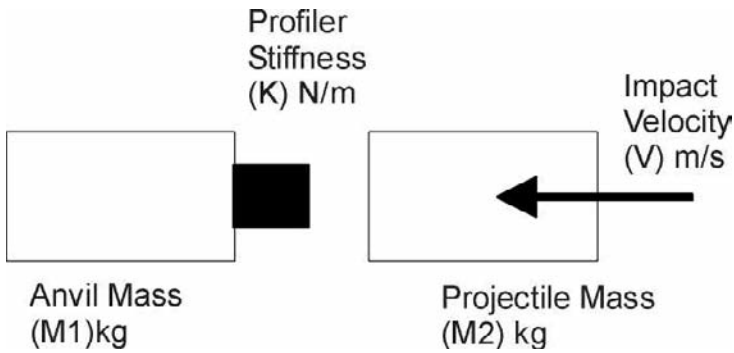

Figure 20: Impact model.

The amplitude of the pulse (A) is independently controlled by the projectile impact velocity (V):

$$A = \frac{\pi}{2} \frac{V}{\tau}$$

4.2 Trials programme

With regard to the scientific payloads carried by the probes, several areas were highlighted, for further investigation, and in particular the use of Solar Array panels on the Mars Hard Lander probe (Burnage and Armstrong, ????) were identified as likely candidates for shock testing. An airgun test configuration was developed in which a carrier anvil was designed so that a segment of the solar array panels (Figure 21) could be attached in a representative manner.

The carrier anvil was mounted in a slotted barrel (Figure 22), and the shock profiler placed within the airgun barrel and in contact with the anvil. Firing the gun drove the piston, which in turn compressed the shock profiler as it reacted against the anvil. The anvil was then propelled along the slotted guide barrel as the stored elastic energy from the shock profiler was released.

A shot of 300 g was performed, followed by the 700 g test case. The magnitudes and durations of the shocks were obtained by varying the impact velocity of the piston and the stiffness and shape of the shock profiler. The anvil was retarded by progressively crushing a 3 m length of aluminium honeycomb located within the slotted tube. Shock responses were measured using an accelerometer mounted on the anvil.

4.3 Test results

The results from the 300 g and 700 g shock tests are presented in Figures 23 and 24 respectively. Following each test, visual inspection revealed that there were no significant

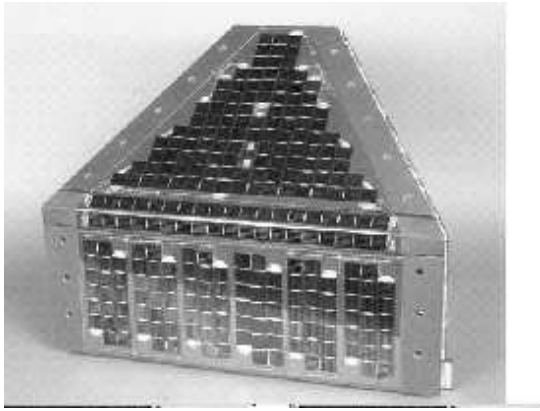

Figure 21: Solar array panels.

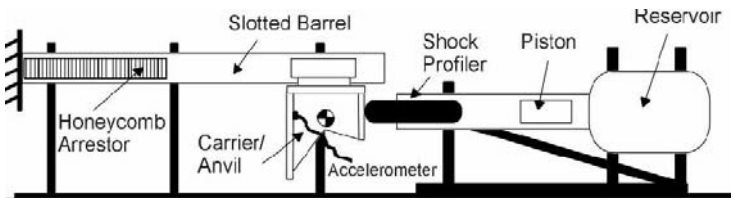

Figure 22: Test Configuration

signs of damage to the supporting structure. The arrays were electronically tested for continuity, and function tested for power generation between each test. Both forms of solar array panels survived the 700 g/18 ms shock test simulation, without any significant degradation to the solar panels.

5 Conclusions

The utility of the instrumentation packaging has been amply demonstrated, despite the numerous restrictions imposed by the geometry of the penetrators and also the magnitude of the applied loading. Interpreting signatures for use in the detection of breaches in protective material, or penetration through layers of differing material has yielded promising results. However, cognisance must be taken in the positioning of the on–board sensors as the acquired data could be readily influenced by the dynamic response of the penetrator.

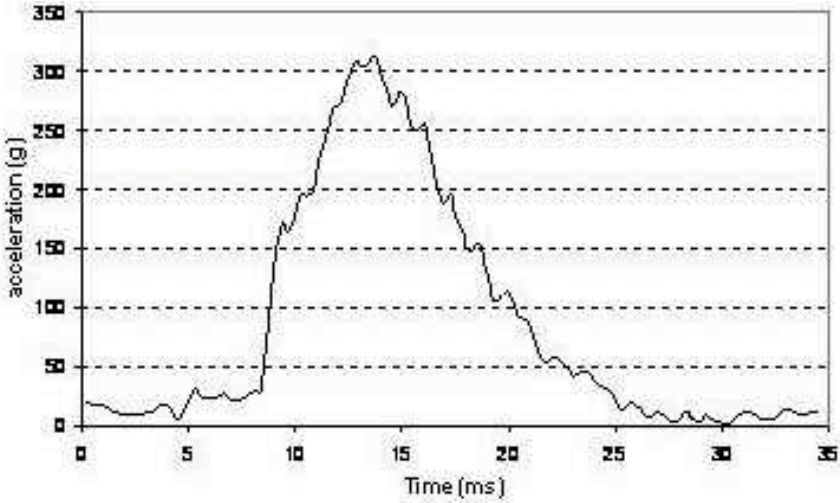

Figure 23: 300 g Half sine test.

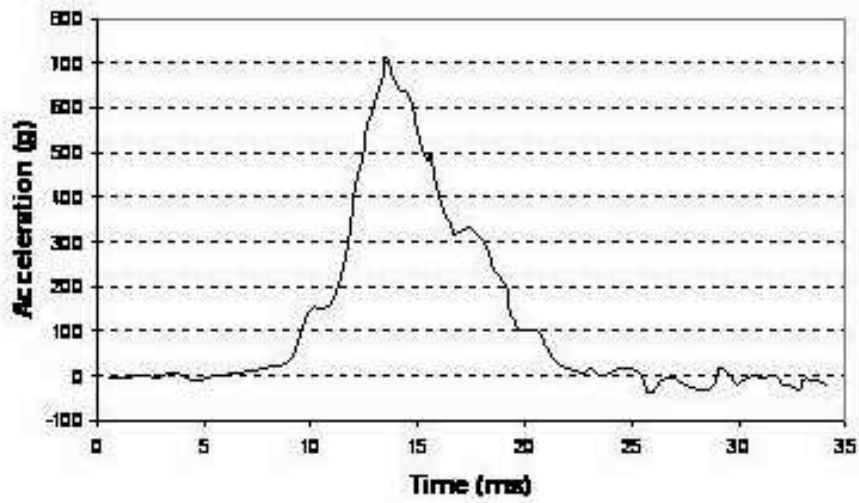

Figure 24: 700 g Half sine test.

References

Young W.C.: Empirical Equations for Predicting Penetration Performance in Layered Earth Materials for Complex Penetrator Configurations. *Sandia Lab. Report SC–DR–72–0523* (1982).

Burnage S., Waine B.: *Penetrator and Hard Lander Probes Technology*. Report to European Space Agency. Contract No. 9840/92/NL/PP(SC) (1993).

User Manual – *Instrument and Engineering Services Inc.*, May 2002.

International Simulation Limited, ISIM User Manual (lic–S 860902) (1992).

Deployment of Micro Rover Access Panel – BepiColombo, Redborne Upper School, HEL/BCTechnology/001 (2000).

Burnage S., Armstrong P.: Solar Arrays for Low Power Applications at Low Intensities. ESA/IPC(91) 24 item no 91 (1994).